

High electrochemical activity of Pd/C catalyst with trace amounts of Pd_xH_y

Minglin Yang^{1,2}, Junwei An^{2,*}, Shichao Zhang³, Lizhen Gao¹, Shaohui Yan^{1,*}

¹ College of Environmental Science and Engineering, Taiyuan University of Technology, Taiyuan, 030024, China

² College of chemistry and chemical engineering, Jining Normal University, Wulanchabu, 012000, China

³ School of Materials Science and Engineering, Beijing University of Aeronautics and Astronautics, Beijing, 100191, China

*E-mail: jwan915@126.com (Junwei An), yanshaohui@tyut.edu.cn (Shaohui Yan)

Received: 16 February 2022 / Accepted: 18 March 2022 / Published: 7 May 2022

A solvothermal method employing a solvent mixed with tert-butyl alcohol and ethylene glycol was used to prepare activated carbon-supported palladium nanoparticles (Pd/C). The transmission electron microscopy (TEM) and high-resolution transmission electron microscope (HRTEM) results showed that the Pd nanoparticles on this catalyst had a good dispersion, and that their average particle size was small. The X-ray diffraction (XRD) data indicated that the Pd nanoparticles loaded on the activated carbon presented a small particle size and were rich in the Pd (200) crystallographic plane, which provided a high electrochemical activity for the Pd/C catalyst. Furthermore, its activity was greatly improved by the small amount of Pd_xH_y components. By analysing the redox peaks of the electrode loaded with the Pd/C catalyst in a KOH and methanol (ethanol) mixed solution via cyclic voltammetry electrochemical testing, the performances of the prepared catalysts were determined. The results showed that the Pd/C catalyst had an excellent activity and stability, while the Pd/C catalyst synthesised at 190 °C had the best activity and stability. Its current intensity for methanol electrooxidation reached approximately 687.4 mA mg⁻¹ Pd. In addition, this catalyst had a stronger oxidation ability for ethanol under alkaline conditions, and its oxidation current intensity of ethanol reached approximately 1177.6 mA mg⁻¹ Pd. The chronoamperometry (CA) results showed that the Pd/C catalyst had an excellent durability, and the electrochemical impedance spectroscopy (EIS) showed that this Pd/C catalyst had an excellent charge transfer efficiency.

Keywords: Pd nanoparticles; Methanol electrooxidation; solvothermal method; Direct methanol fuel cells; Electrocatalysis

1. INTRODUCTION

Direct methanol fuel cells have outstanding advantages in terms of effect, energy savings, pollution reduction, transportation, and storage, and have broad application prospects in new energy vehicles and mobile electrical equipment [1-3]. The demand for direct methanol fuel cells is increasing, and electrochemical catalysts are one of the key components of methanol fuel cells [4]. As the most mature electrochemical oxidation catalyst in alcohol fuel cells, Pt-based catalysts have a high activity and good stability [5, 6]. However, Pt-based catalysts have obvious defects; for example, in the catalytic oxidation of methanol, the active sites of Pt-based catalysts are easily occupied by the intermediate product CO [5,7], forming a poisoning reaction and hindering further oxidation [8,9]. In addition, the scarcity of Pt resources on Earth has resulted in the high price of Pt, which affects the manufacturing cost of Pt-based catalysts and restricts the possibility of large-scale industrial production [10-13]. Researchers have currently shifted from optimizing Pt-based catalysts to finding other high-performance and cheap metals to replace Pt [14-16].

In recent years, Pd-based catalysts have been extensively studied as excellent alternative materials for Pt-based catalysts [17-19]. As a platinum-based element, Pd has a similar electronic configuration to Pt. Pd is widely used in the aerospace, aviation, and automobile manufacturing industries due to its low price [20-22]. In addition, a large number of studies have shown that Pd-based catalysts have an outstanding performance in the catalytic oxidation of methanol under alkaline conditions [23-25].

The preparation methods of Pd-based catalysts have been proposed in large numbers, such as plasma sputtering technology [26,27], electrostatic self-assembly and the in situ reduction method [28], electrical displacement method [29], electrodeposition method [30], chemical reduction method [31], polyol process [32], colloid method [33], etc. Synthesised Pd-based catalysts also have an excellent performance. However, most methods have the disadvantage of not being industrialised in large quantities. The preparation method affects the particle size, structure, and composition of the noble metal nanoparticles, thereby affecting the performance of the catalyst [34,35].

The solvothermal method has been widely studied for its convenient operation, stable product performance and suitability for large-scale production [36,37]. Tert-butanol, as a catalyst for the preparation process, can also provide guidance for the formation of nanoparticles, with appropriate molecular structure hydrophobicity, as well as the required solution viscosity during the reaction process, which is usually used as a preparation solvent [38,39]. However, studies have shown that Pd-based catalysts prepared by the solvothermal method of tert-butyl alcohol have a large nanoparticle size [39]. At the same time, studies have shown that the nanoparticle size of the product prepared by the microwave method using ethylene glycol as another reducing agent is significantly smaller [40].

Pd was one of the few metals capable of forming metal hydrides. The entry of H leads to the lattice expansion of Pd, which causes a change in the lattice constant, resulting in a superior performance in the field of catalysis [41]. The main methods reported to synthesise Pd_xH_y were as follows: 1. Direct exposure of Pd to H₂ via adsorption of gaseous H₂ into H₂ under a high pressure [42]. 2. Preparation of electrochemical hydrogen evolution [43]. 3. Solvothermal methods using dimethylformamide (DMF)

[44], sodium borohydride (NaBH_4) [45] and formaldehyde (HCHO) [46] as H sources. According to our study, tertiary-butyl alcohol [47] can also provide H during high-temperature heating.

To improve the activity and anti-poisoning performance of the Pd catalyst, the crystal plane distribution and the average particle size of Pd nanoparticles in the Pd/C catalyst were optimised in this study. Based on the ethylene glycol reduction method, a series of Pd/C catalysts were synthesised at 160–190 °C with tert-butyl alcohol as the initiator, and their catalytic ability for methanol oxidation was studied.

2. EXPERIMENTAL

2.1 Synthesis of the catalysts

A solvothermal method was used to prepare the Pd/C catalyst. The specific preparation methods were as follows: 0.048 g of pretreated activated carbon were mixed with 2 ml of a 0.0564 M PdCl_2 solution, 5 ml of ethylene glycol and 35 ml of tert-butyl alcohol in a 100 ml beaker. The beaker was stirred with ultrasonication for 25 min. To adjust the pH of the mixed solution, 5 ml of a 1 M KOH liquid solution was added to the mixed solution above. After the mixed solution was stirred with ultrasonication for 5 min, the mixed solution was poured into a stainless-steel reactor with a polytetrafluoroethylene liner, which was heated at 190 °C for 6 h. For a comparison, other Pd/C catalysts were synthesised using the same conditions, except that the reaction was performed at 160, 170, 180, and 200 °C. After cooling the stainless-steel reactor to room temperature, the mixed solution was diluted with anhydrous ethanol. The Pd/C catalysts were collected via vacuum filtration, and the samples were thoroughly washed with distilled water. After drying the sample in a vacuum oven at 60 °C for 6 hours, the dried samples were ground with an agate mortar and stored in a plastic centrifuge tube. Finally, a Pd/C catalyst was obtained. The prepared catalyst was denoted Pd/C-a, in which the value of “a” represents the preparation temperature of the reaction system. Thus, the catalysts were labelled Pd/C-160, Pd/C-170, Pd/C-180, Pd/C-190 and Pd/C-200.

2.2 Characterization of the Pd/C catalysts

The metal content of the Pd/C catalyst was measured using a PinAAcle 900 (PerkinElmer, PERKINELMER SINGAPORE PTE. LTD.) atomic absorption spectrometry (AAS). The morphologies of the Pd/C catalyst supported on activated carbons were characterised using JEM 1200EX (JEOL Company, JPN) and Tecnai G2 F30 S-TWIN (FEI Company, USA) TEM devices. X-ray diffraction (XRD) patterns were obtained on a BRUCKER D8 wide-angle goniometer employing a Cu target with radiation $K_{\alpha} = 0.15418$ nm and a scanning range (2 theta) from 5° to 90° at 5°/min with a scan step length of 0.02/s.

2.3 Electrochemical measurements

Electrochemical data were tested using a CHI760E electrochemical workstation (Shanghai Chenhua Instrument Co., LTD) in a three-electrode system at room temperature, with a saturated Ag

[AgCl electrode as the reference electrode and a graphite electrode (4 cm²) as the counter electrode. The glassy carbon electrode ($\Phi = 4$ mm) modified by the Pd/C catalysts was used as the working electrode, which was fabricated according to the literature [48,49]. A 0.5 M H₂SO₄ solution was used as the acid test electrolyte, with the aim of determining the electrochemical surface area of the catalysts. To test the electrochemical activities for the methanol and ethanol oxidations, 0.1 M KOH/1 M CH₃OH and 0.1 M KOH/1 M CH₃CH₂OH mixed solutions were used as the alkaline test solutions. High purity nitrogen was inflow into those solutions in order to remove the dissolved oxygen in the electrolytes while keeping the temperature at 25 °C before all of the electrochemical tests.

3. RESULTS AND DISCUSSION

3.1 Characterization of the Pd/C catalysts

As shown in Table 1, the AAS analysis demonstrated that the actual Pd nanoparticle loadings of the Pd/C-190 catalyst were the highest among these catalysts. Moreover, the actual Pd loading of the as-prepared Pd/C catalyst was lower than the theoretical loading, illustrating that Pd²⁺ was not completely reduced. It was not difficult to see that the loading of Pd nanoparticles first increased and then decreased with an increasing reaction temperature. As a result, the loading efficiency of the Pd nanoparticles in the Pd/C-190 catalyst was higher than that in the other catalysts. The reason for this phenomenon may be related to the reaction mechanism. As a reducing agent, tertiary-butyl alcohol and ethylene glycol generated reducing intermediate substances under alkaline conditions at a high temperature [38,50-52]. However, tertiary-butyl alcohol decomposed and lost its reducing property when the temperature was increased further [39,53].

Therefore, the reducing intermediate substances first increased and then decreased with an increasing temperature, leading to the reduction rate first increasing and then decreasing with temperature. This resulted in the Pd loading of the Pd/C catalyst being raised when the temperature was lower than 190 °C. In this preparation process, the optimal reaction temperature was 190 °C, under which the Pd nuclei were loaded on the activated carbon quickly, massively, and uniformly, thereby forming a highly Pd-loaded catalyst. When the reaction temperature was higher than 190 °C, the nucleation rate was affected, which caused the Pd loading of the Pd/C-200 catalyst to be lower than that of the Pd/C-190 catalyst [23,52,54].

Table 1. Pd loading of the Pd /C catalysts measured by AAS

Catalyst	Actual loading (wt%)	Theoretical loading (wt%)
Pd/C-160	16.5%	20%
Pd/C-170	16.9%	20%
Pd/C-180	17.1%	20%
Pd/C-190	17.4%	20%
Pd/C-200	16.6%	20%

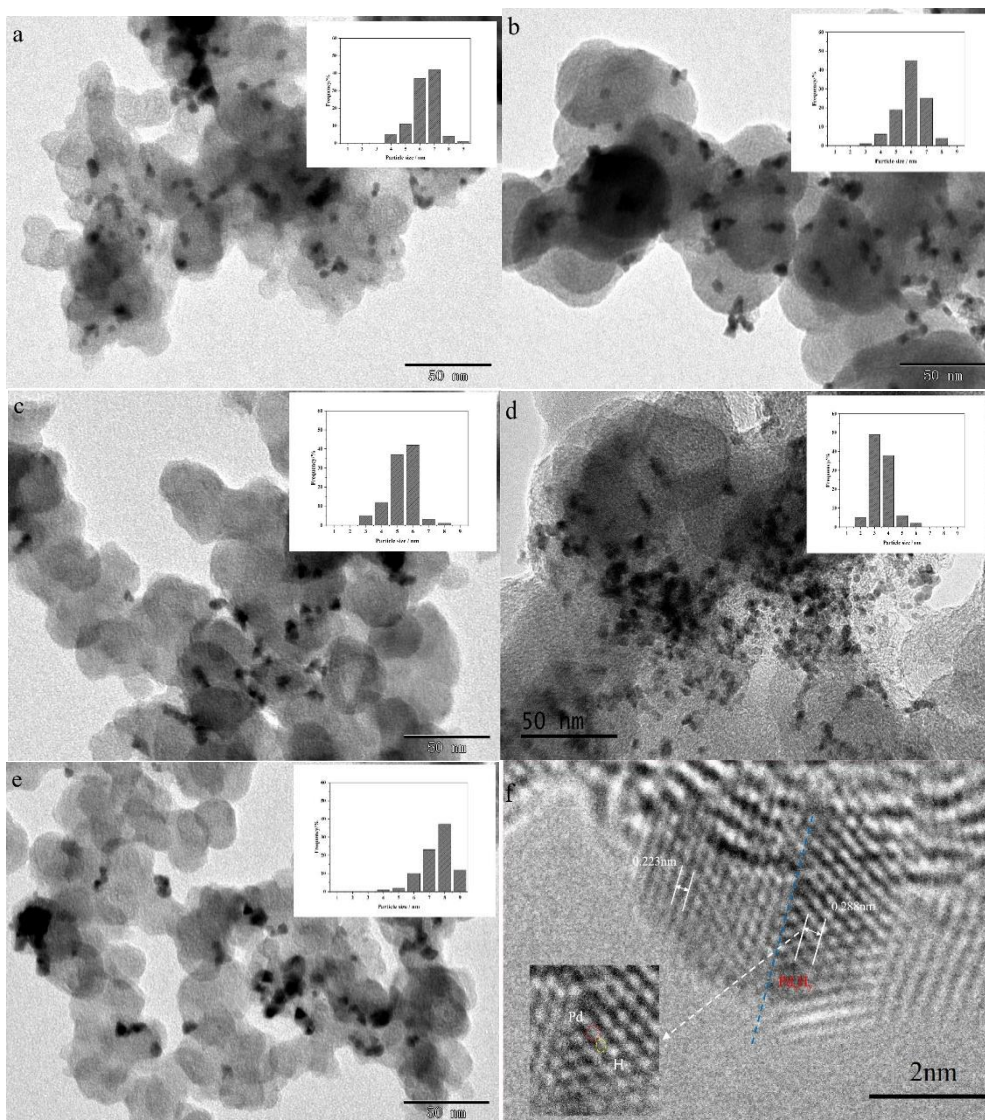


Figure 1. TEM images of the Pd/C -160 (a), Pd/C -170 (b), Pd/C -180 (c), Pd/C -190 (d) and Pd/C -200 (e) catalysts. The HRTEM image of the Pd nanoparticle in the Pd/C -190 catalyst (f). The inset in Fig. 1 (f) showed the distribution of the Pd and H atoms in the Pd_xH_y component.

The morphologies of the Pd nanoparticles in the Pd/C-160 (a), Pd/C-170 (b), Pd/C-170 (c), Pd/C-190 (d) and Pd/C-200 (e) catalysts are shown in Fig. 1. The diameters of the Pd/C-160 (a), Pd/C-170 (b), Pd/C-180 (c), Pd/C-190 (d) and Pd/C-200 catalysts were 6.32 nm, 5.99 nm, 5.29 nm, 3.51 nm, and 3.84 nm, respectively. It can be seen from the TEM images that the Pd/C catalysts had Pd nanoparticles with a uniform distribution, proving that it was feasible to prepare Pd/C via the solvothermal method using a mixed solution of ethylene glycol and tert-butanol. It can also be seen that the mean particle size of the Pd nanoparticles loaded on activated carbon decreased gradually with temperature. The most likely reason for this result was that the rising temperature and the increasing intermediate reducing substances produced by ethylene glycol and tert-butyl alcohol accelerated the nucleation rate, thus forming smaller

Pd nanoparticles [55]. However, when the temperature reached 200 °C, the Pd nanoparticles formed large agglomerated particles, and the particle size of the nanoparticles increased sharply. The possible reason for this was that the decomposition of tertiary-butyl alcohol leads to a decrease in the reducibility and a sharp reduction in the number of crystal nuclei, which is one of the most important reasons for the increase in the particle size of nanoparticles [56].

Therefore, Pd/C-190 (d) was a catalyst with a uniform dispersion and the smallest nanoparticle size prepared by this experimental method, and the temperature had a great influence on the preparation of the Pd/C catalyst. Compared with the particle size (9.85 nm) of the Pd/C catalyst prepared by using tert-butanol as a reducing agent [39], the particle size optimization was obvious. The reason was that, in the solvothermal process, ethylene glycol, as a stabiliser, inhibited the growth of in situ-generated Pd nanoparticles, while activated carbon provided nucleation sites for Pd nanoparticles to prevent the aggregation of Pd nanoparticles [50,57].

The HRTEM of the Pd nanoparticle in the Pd/C -190 catalyst was shown in Fig. 1 (f). It was obvious that the lattice spacings of the Pd nanoparticles in Fig. 1 (f) were 0.288 and 0.223 nm, respectively, in two fully separated regions, in which the boundary is denoted by the blue dashed line. 0.223 nm corresponded to the (111) spacing of Pd on the left of the blue dashed line. At the same time, lattice deformation along the boundary was observed on the Pd (111) crystal plane in Fig. 1 (f), which would enhance its electrochemical activity [58]. However, the lattice spacing with 0.288 nm on the right of the blue broken line was consistent with the Pd_{1.5}H₂ (111) crystal plane. The lattice distribution was similar to that of the Pd (111) crystal plane, but the lattice spacing was much larger than that of the Pd (111) crystal plane. In this area, a small atom, which is presented by the yellow dotted circle, can clearly be seen beside a large atom in the red dotted circle, showing that other atoms were doped in the crystal lattice. According to a previous study, hydrogen gas, which was produced in situ by aldehydes generated by tert-butyl alcohol at high temperatures under alkaline conditions on metal catalysts [58], which was absorbed into the Pd nanocrystals to form Pd_xH_y at a high pressure [47]. In the meantime, the small atoms were hydrogen atoms, which resulted in lattice expansion. This result was consistent with the literature [47]. Lattice expansion occurred in the product, resulting in an increase in the Pd atom distance. There was obvious lattice distortion between Pd and Pd_xH_y, which led to a local lattice strain because the dislocation or deviation of the Pd atoms from their initial positions was due to structural defects [59-61]. Meanwhile, a small amount of Pd_xH_y may be synthesised on Pd nanoparticles, which also contributed to the performance of the Pd/C-190 catalyst.

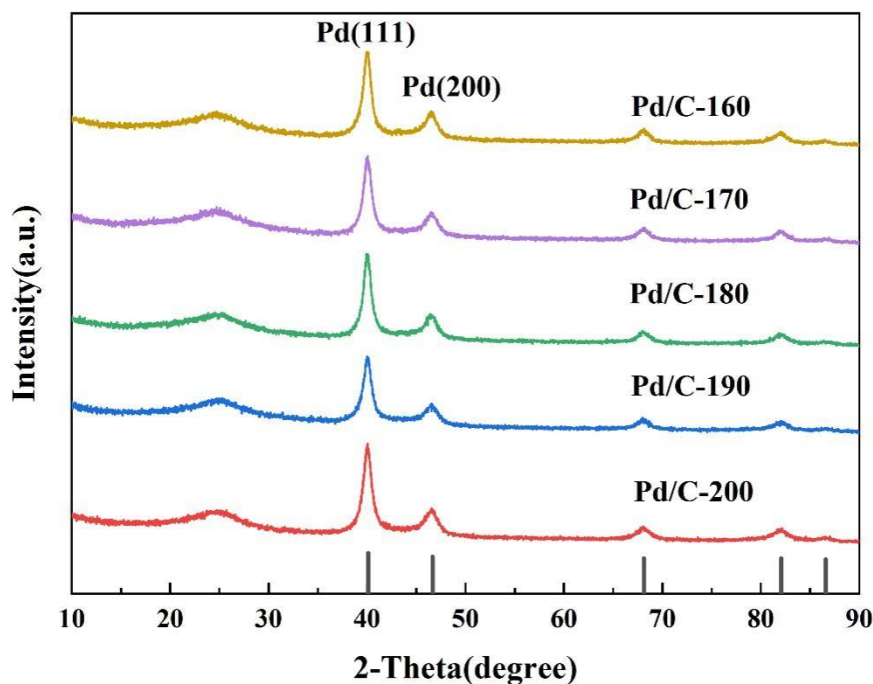
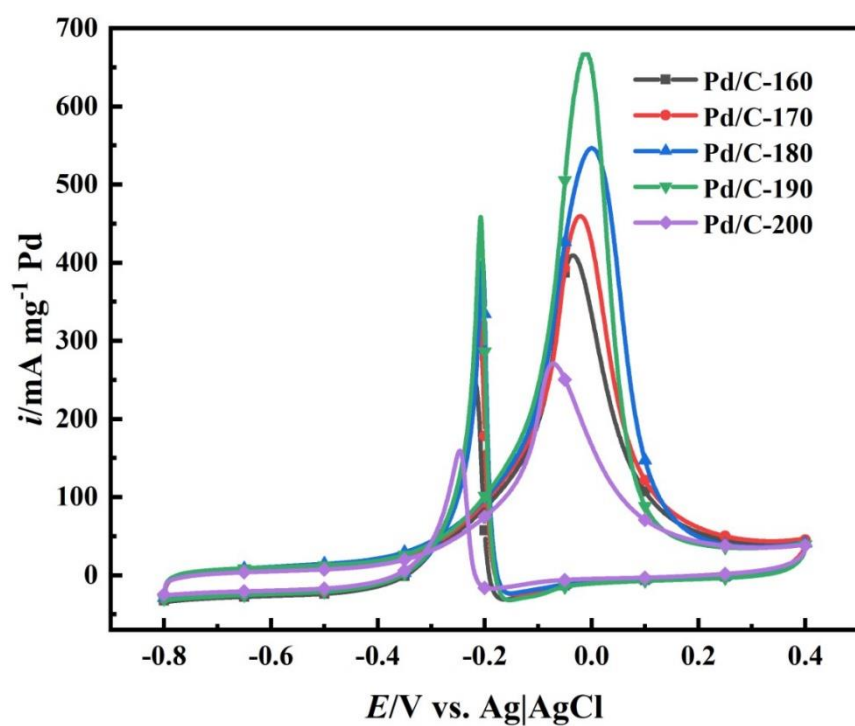


Figure 2. XRD spectra of the Pd/C -160, Pd/C -170, Pd/C -180, Pd/C -190 and Pd/C -200 catalysts.

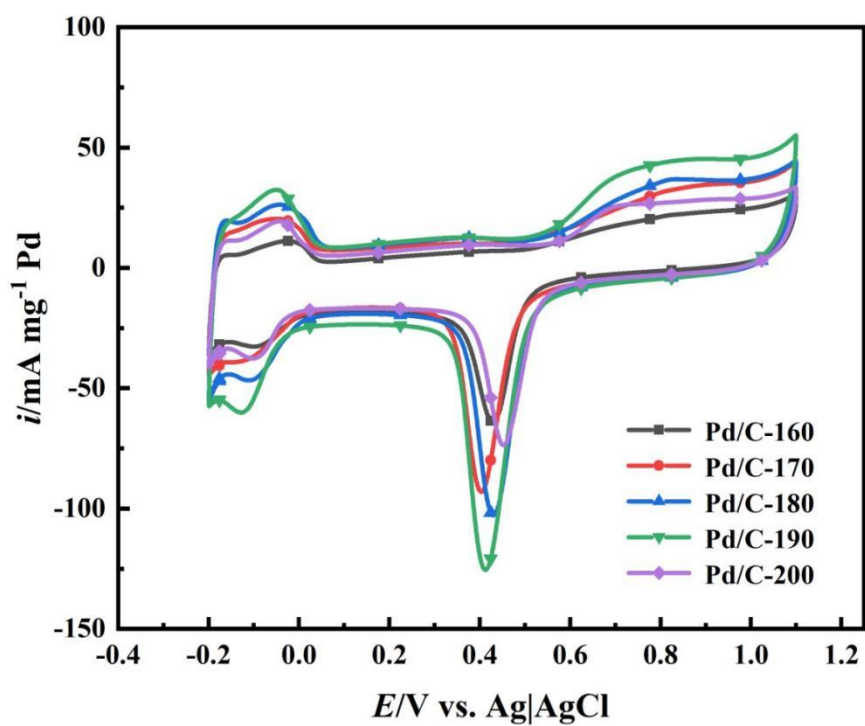
The composition and structure of the Pd/C-160, Pd/C-170, Pd/C-180, Pd/C-190, and Pd/C-200 catalysts were characterised via XRD, as shown in Fig. 2. There was a large diffraction peak in all XRD images from $2\theta = 15^\circ$ to $2\theta = 33^\circ$, which was related to the diffraction of the carbon carrier (JCPDS, No. 50.926). The diffraction peaks near $2\theta = 40.2$, 46.8 , 68.2 , 81.9 and 86.6° correspond to the Pd (111), (200), (220), (311) and (222) lattice planes, respectively [62]. One of the important parameters for the Pd lattice structure was the intensity ratio between the diffraction peaks of different planes. According to the XRD data, the average strength ratios of the Pd (200) to Pd (111) lattice planes of the Pd/C-160, Pd/C-170, Pd/C-180, Pd/C-190 and Pd/C-200 catalysts were 0.357, 0.369, 0.383, 0.405 and 0.388, respectively. The average strength ratio of the Pd (200) to Pd (111) lattice plane of the Pd/C-190 catalyst was the highest, which was close to the strength ratio (≈ 0.42) calculated by the standard Pd XRD card (JCPDS, No. 5-0681). This meant that the number of Pd (200) lattice planes for the Pd/C-190 catalyst were greater than those for the other catalysts, which was also one of the reasons why the Pd/C-190 catalyst had a higher electrochemical activity. The existence of Pd_xH_y can be seen by the TEM of Fig. 1f, but there was no diffraction peak in the XRD patterns. Presumably, ethylene glycol coated on the surface of Pd nanoparticles prevented the binding of Pd and H, which led to the amount of Pd_xH_y being too low to be detected by XRD.

3.2 Electrochemical analysis of Pd/C nanocatalysts

a



b



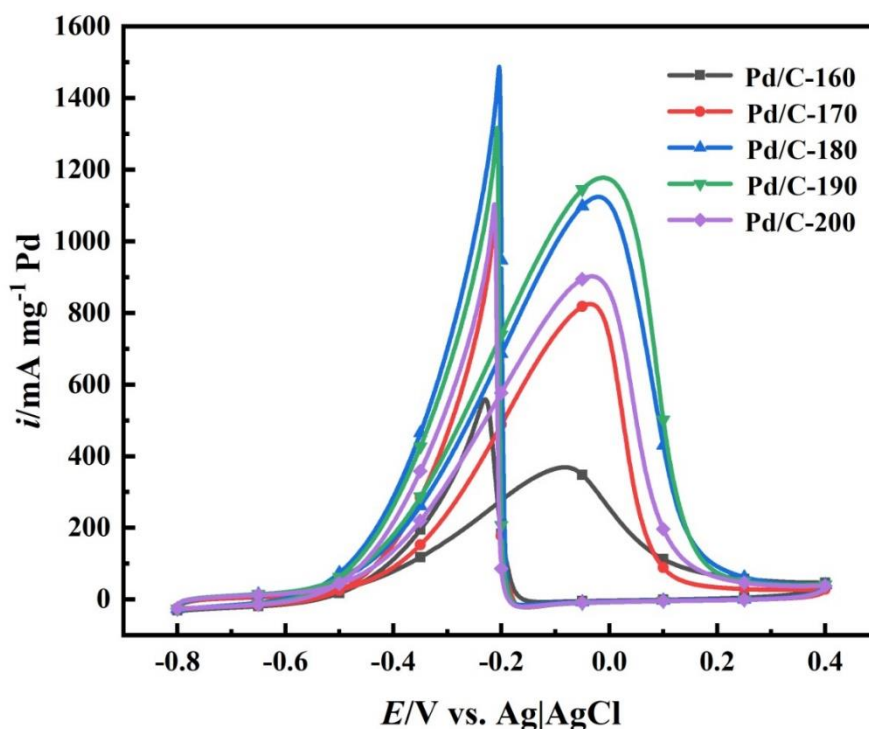
c

Figure 3. CVs of the Pd/C -160, Pd/C -170, Pd/C -180, Pd/C -190 and Pd/C -200 catalysts in 0.1 M KOH + 1 M CH₃OH (a), 0.5 M H₂SO₄ (b) and 0.1 M KOH + 1 M CH₃CH₂OH (c) at the scan rate of 50 mV s⁻¹. (The 30th cycle)

All cyclic voltammograms (CVs) in Fig. 3 were obtained via cyclic voltammetry tests at room temperature (25 °C) in a 0.1 M KOH + 1 M CH₃OH solution at a scan rate of 50 mV s⁻¹. As shown in Fig. 3 (a), the cyclic voltammograms (CVs) of the Pd/C catalysts showed that methanol began to be oxidised near -0.5 V, and the maximum anodic current density generated by each catalyst test was between -0.1 V and 0 V. The Pd loadings measured by AAS were used to normalise the data. Fig. 3 (a) shows that the maximum current densities of the Pd/C-160, Pd/C-170, Pd/C-180, Pd/C-190, and Pd/C-200 catalysts were 409.2, 459.8, 547.7, 687.4, and 276.4 mA mg⁻¹Pd, respectively. Obviously, the anode current densities generated by these Pd/C catalysts first increased and then decreased, and the current density on the Pd/C-190 catalyst test at -0.02 V was the highest among these Pd/C catalysts. Obviously, the change trend of these mass specific current densities with the reactor temperature was associated with those of the mean Pd particle size and the Pd loading with temperature because the small particle size and high Pd loading provided abundant active sites for the electrochemical reaction [50]. Otherwise, the unit active site had a great activity for Pd nanoparticles with small diameters due to the size effect [40]. The excellent electrochemical performance of the Pd/C-190 catalyst was also attributed to the good dispersion of the Pd nanoparticles in the Pd/C-190 catalyst because the high dispersion reduced the accumulation of intermediates in the methanol electrooxidation reaction on the surface of the Pd nanoparticles, making methanol more easily adsorbed on the electrode surface [63]. In addition, another

reason why the Pd/C-190 catalyst had a greater activity compared to the other Pd/C catalyst was possibly related to the amount of the Pd (200) crystal surface, which greatly contributed to improving the electrochemical activity [64,65]. However, the anode current density of the Pd/C-200 catalyst markedly decreased because the Pd nanoparticles of the Pd/C-200 catalyst agglomerated.

As demonstrated in Fig. 3 (b), the maximum current densities tested in the 0.1 M KOH + 1 M CH₃CH₂OH solution of the Pd/C-160, Pd/C-170, Pd/C-180, Pd/C-190, and Pd/C-200 catalysts were 369.0, 824.7, 1124.1, 1177.6, and 902.3 mA mg⁻¹Pd, respectively. The activity of the Pd/C-190 catalyst was also the best among these Pd/C catalysts for ethanol electrochemical oxidation, which was caused by its small Pd nanoparticles with a good dispersion and a quantity of Pd (200) crystal planes. The reason why the high-index lattice plane, such as the Pd (200) lattice plane, improved the activity may be because the increase in the Pd atom spacing made the Pd (200) lattice plane provide more active sites than the Pd (111) lattice plane [66].

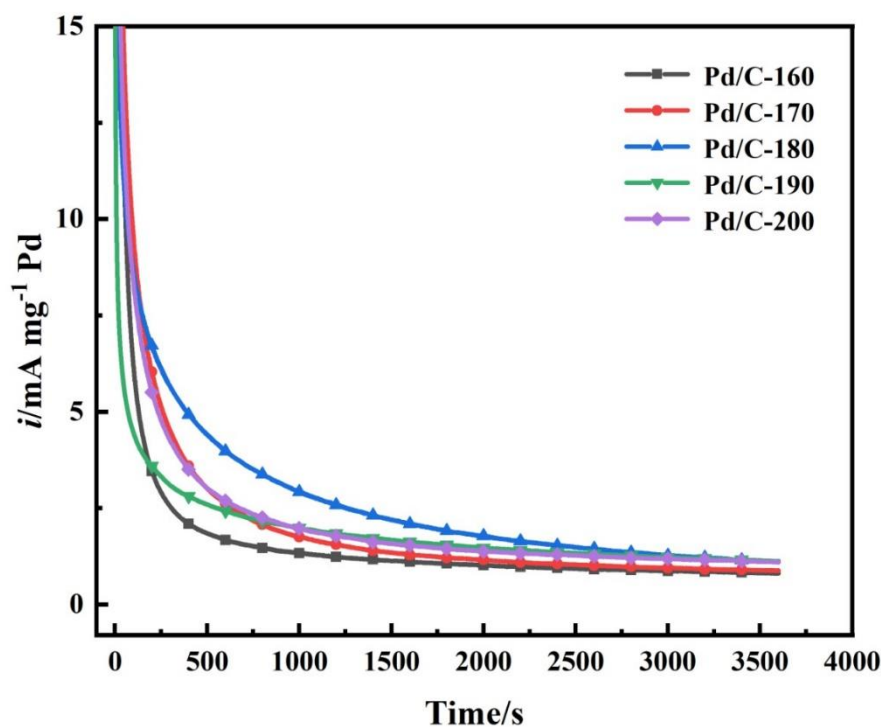
Otherwise, the Pd/C-190 catalyst had a much higher electrochemical activity than the Pd/C catalyst reported in the literature [50]. This was relevant to the essential characteristics of the Pd/C-190 catalyst. In addition to the merits of the small Pd nanoparticles, the high dispersion of the Pd nanoparticles, and the abundant Pd (200) lattice face, the Pd_xH_y component in the Pd/C catalyst was another important factor [45]. First, the carrier mobility was increased due to the lattice distortion induced by Pd_xH_y [67]. The interaction between H and Pd led to the split band of Pd, and the d-band centre of Pd decreased. The downwards movement of the d-band centre of Pd weakened the bond interaction between Pd and the reaction adsorbate, thereby improving the electrocatalytic performance [44]. Second, the Pd_xH_y component had more active sites [68]. The reason was that the interstitial hydrogen atoms increased the electronic density, enlarged the bond distance, and lowered the coordination number of the Pd atoms [69]. Moreover, the increase in the Pd atom spacing improved the utilization of Pd atoms, which was similar to the Pd (200) lattice faces having more active sites. Third, the chemical state of the Pd atom in Pd_xH_y was another possible reason. As shown in Fig. 3 (b), the reduction potential of PdO was higher than that for H₂O, indicating that the bonding force between H and O is stronger than that between Pd and O. This illustrated that the electronegativity of H was stronger than that of Pd, resulting in negatively charged Pd ions. It was reported that the activity of low-valent Pd was better than that of high-valent Pd [39,68,70]. Therefore, the Pd/C-190 catalyst with the Pd_xH_y component had a much better activity than the common Pd/C catalysts. For the preparation of the Pd/C catalysts, the small Pd nanoparticles and the high Pd loading of the Pd/C catalyst depended on the action of ethylene glycol, which was employed as a stabiliser in the reaction system, while the Pd_xH_y component in the Pd/C catalyst was contributed to by the tert-butyl alcohol reactant, which provided the H source for generating Pd_xH_y. Consequently, the mixture of tert-butyl alcohol and ethylene glycol was a perfect solvent combination to synthesise the Pd/C catalyst with high electrochemical activity.

As shown in Fig3 (b), the CVs of the Pd/C catalysts in the 0.5 M H₂SO₄ solution had a cathodic current peak as the reduction peak generated by Pd oxide from 0.25 to 0.55 V [39]. The electrochemical active surface area (ECSA), an important indicator of catalyst activity, can be calculated by the cathodic current peak, according to the following equation [70].

$$\text{ECSA} = Q / [\text{Pd}] * 0.424 \quad (1)$$

Which “Q” is the charge collected from 0.25 to 0.55 V, which was proportional to the cathode peak area shown in Fig. 3 (b). The result showed that the electrochemical active surface areas of the Pd/C-160, Pd/C-170, Pd/C-180, Pd/C-190, Pd/C-200 catalysts were 306.5, 344.3, 403.9, 469.0 and 303.6 $\text{cm}^2 \text{mg}^{-1} \text{Pd}$, respectively. It can be concluded that the ECSA of the Pd/C-190 catalyst is the largest because the Pd nanoparticles in the Pd/C-190 catalyst had a small size and a good dispersibility [72], which was consistent with the TEM results. This further confirmed the conclusion that Pd/C-190 had the best catalytic activity among these catalysts. According to the ECSAs of the Pd/C catalysts, the electrocatalytic specific surface current densities of the Pd/C-160, Pd/C-170, Pd/C-180, Pd/C-190, Pd/C-200 catalysts were 1.33, 1.34, 1.36, 1.47 and 0.91 mA cm^{-2} , respectively. By comparison, the current density of the Pd/C-190 catalyst was the highest among these catalysts, showing that the activity of its single active site was better than that of the active site in another catalyst. There are two reasons for the high activity of the single active site in the Pd/C-190 catalyst. On the one hand, the number of Pd (200) lattice planes for the Pd/C-190 catalyst was greater than those for the other catalysts, which was also one reason why the Pd/C-190 catalyst had a higher specific surface activity. The further reason was that the Pd (200) lattice plane provided more adsorption sites than the Pd (111) lattice plane in the electrochemical reaction [73,74]. On the other hand, there were more Pd_xH_y components in the Pd nanoparticles of the Pd/C-190 catalyst than in the other catalysts, which was led by its small Pd nanoparticles. The possible reason was that the surface of the small Pd nanoparticles was more easily combined with H to yield Pd_xH_y components than the large Pd nanoparticles on the Pd nanoparticle surface due to the size effect [59].

a



b

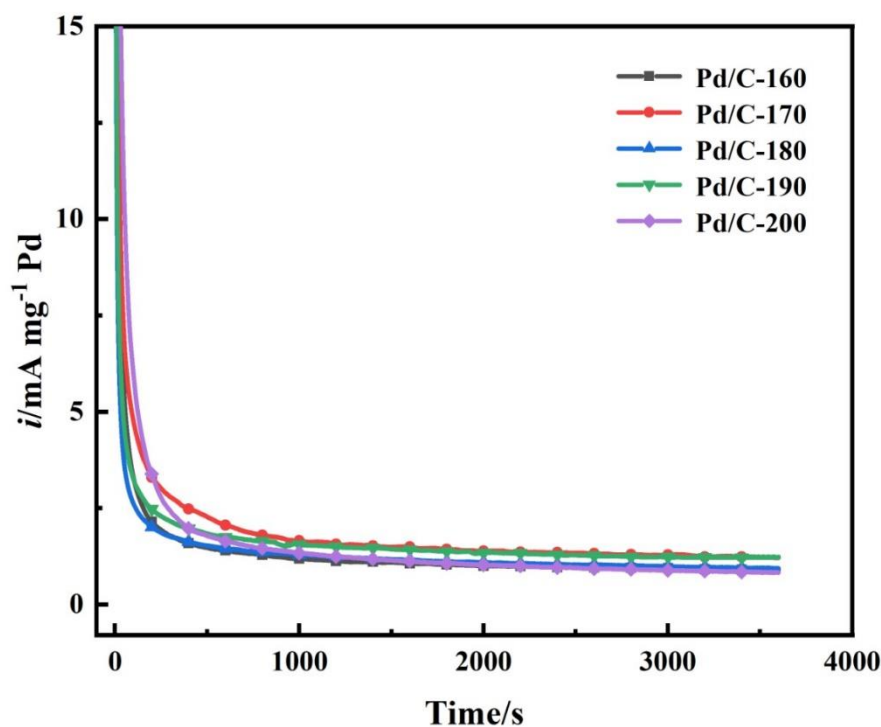


Figure 4. Chronoamperometric curves run at -0.02 V vs. Ag|AgCl on the Pd/C-160, Pd/C-170, Pd/C-180, Pd/C-190 and Pd/C-200 catalysts respectively in the mixed solutions of 0.1 M KOH + 1 M CH_3OH (a) and 0.1 M KOH + 1 M $\text{CH}_3\text{CH}_2\text{OH}$ (b) for 3600 s at 25 °C.

As a reliable and important method for verifying the stability of catalysts, chronoamperometry is often used in electrochemical fields [63] under at -0.02 V, where the electrode loaded with the Pd/C catalyst was subjected to 3600 s for the chronoamperometry test. As shown in Fig. 4, the current of the catalyst tended to be stable after 3600 s. The current densities at 3600 s for the Pd/C-160, Pd/C-170, Pd/C-180, Pd/C-190 and Pd/C-200 catalysts in the 0.1 M KOH + 1 M CH_3OH solution were 0.80 , 0.89 , 1.10 , 1.12 and 1.10 mA mg^{-1} Pd, respectively. In the 0.1 M KOH + 1 M $\text{CH}_3\text{CH}_2\text{OH}$ solution, the current densities of the Pd/C-160, Pd/C-170, Pd/C-180, Pd/C-190 and Pd/C-200 catalysts at 3600 s were 0.89 , 1.21 , 0.94 , 1.24 and 0.83 mA mg^{-1} Pd, respectively. From Fig. 4, the current density decreased sharply in the initial stage and then stabilised gradually in the later stage. The reasons were as follows: in the initial stage, the catalysts had sufficient active sites to catalyse the alcohol oxidation reaction. As the reaction proceeded, however, the intermediates accumulated and occupied the active sites of the Pd/C catalyst, resulting in a rapid decrease in the current density and a decrease in the catalytic performance [75]. It can be concluded that the Pd/C-190 catalyst had the best electrocatalytic stability in this series of catalysts and possessed an excellent CO-like tolerance because the small particle size and good dispersion of the Pd nanoparticles in the Pd/C-190 catalyst made outstanding contributions to the diffusion of CO-like intermediates from its surface [76].

Table 2. EIS parameters of the catalysts

Catalyst	0.1 M KOH + 1 M CH ₃ OH				0.1 M KOH + 1 M CH ₃ CH ₂ OH			
	R1/ohm	R2/ohm	CPE1T/μF	CPE1P/μF	R1/ohm	R2/ohm	CPE1T/μF	CPE1P/μF
Pd/C-160	57.01	1497	0.00021946	0.94513	64.75	1273	0.00027029	0.90257
Pd/C-170	64.67	1744	0.00021933	0.93043	58.32	2695	0.00020927	0.91856
Pd/C-180	61.58	5855	0.00021729	0.92082	54.15	1775	0.00018446	0.92032
Pd/C-190	65.07	1217	0.00020553	0.96478	29.47	563.8	0.00047968	0.86526
Pd/C-200	58.27	5743	0.00025453	0.92816	54.35	1878	0.00021773	0.91975

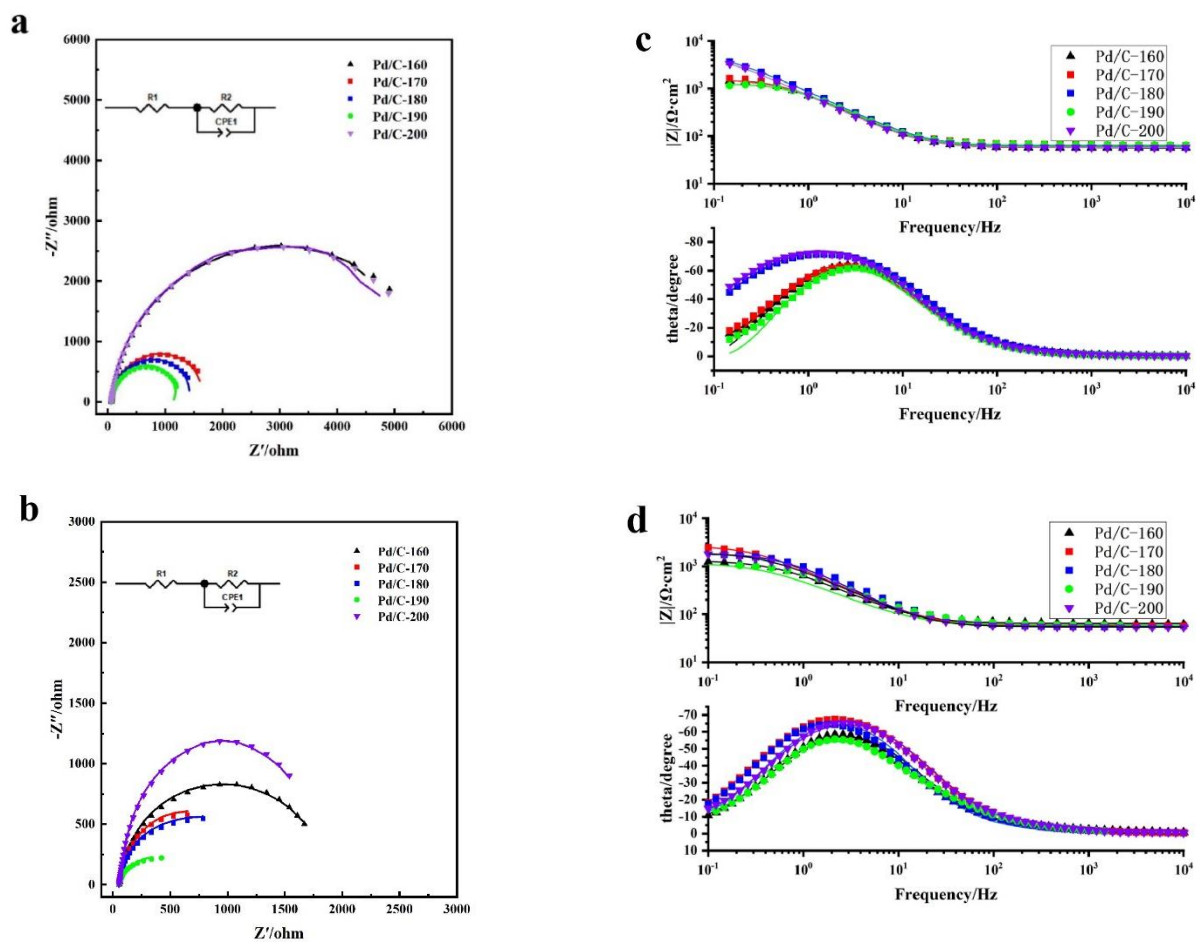


Figure 5. Nyquist plots and Bode plots of electrooxidation on the Pd/C-160, Pd/C-170, Pd/C-180, Pd/C-190 and Pd/C-200 catalysts in ((a) and (c)) 0.1 M KOH + 1 M CH₃OH and ((b) and (d)) 0.1M KOH + 1M CH₃CH₂OH at -0.02V vs. Ag|AgCl.

Electrochemical impedance spectroscopy (EIS) can be used to analyse electrode materials and electrode reaction kinetics. The prepared catalysts were analysed via electrochemical impedance spectroscopy at -0.02 V from 100 k to 0.01 Hz in the 0.1 M KOH + 1 M CH₃OH and 0.1 M KOH + 1 M CH₃CH₂OH solutions. The equivalent circuit model was constructed to fit the data. The corresponding data are listed in Table 2 and shown in Fig. 5. R1 represents the solution resistance, and R2 represents the charge transfer resistance, which is the resistance produced by the gain and loss electrons in the electrode reaction and is largely dependent on the difficulty of the electrode material itself [77]. For the EIS data, different catalysts led to different degrees of difficulty in obtaining and losing electrons on the electrode surface, and the reaction rate of methanol or ethanol oxidation can be determined from the radius in the EIS figure [78]. As shown in Fig. 5, the electrochemical impedance radius first decreased with an increasing catalyst preparation temperature and then increased rapidly. Bode plots (Figs. 5 (c) and (d)) exhibited three distinctive segments. In the higher frequency region with an increasing frequency, the $\log |Z|$ values tended to become minimum values, and the phase angle values fell rapidly towards 0° . In the medium frequency region, a linear relationship can be observed between $\log |Z|$ against \log frequency, with a slope near -1 and the phase angle tending towards -90° . In the low-frequency region, the resistive behaviour of the electrode increases, but the region where $\log |Z|$ does not depend on \log frequency, i.e., the direct current limit, is not completely reached [79]. The results indicate that the Pd/C-190 catalyst had the smallest electrochemical impedance radius, concluding that the Pd/C-190 catalyst had the fastest charge transfer among these catalysts due to the small size, good dispersion and abundant Pd (200) crystal faces of the Pd nanoparticles with the Pd_xH_y component in the Pd/C-190 catalyst [50]. Interestingly, the impedance radius shown in Fig. 5 was roughly equal to half of R2 listed in Table 2. As shown in Fig. 5, the relationship between the real part (Z_{Re}) and the imaginary part (Z_{Im}) of the impedance in the equivalent circuit diagram was as follows [80]:

$$(Z_{Re}-R_1-R_2/2)^2+Z_{Im}^2=(R_2/2)^2 \quad (2)$$

Plotting this formula, a semicircle with a radius of $R_2/2$ is obtained. The radius was equal to the value of $R_2/2$, which proved that the optimal fitting data were obtained [81].

4. CONCLUSIONS

A simple and industrialised hydrothermal synthesis method of the Pd/C catalyst using mixed ethylene glycol and tert-butanol as mixed solvents was explored, achieving good results. The characterization showed that the Pd nanoparticles were successfully loaded onto activated carbon with a good dispersion. The Pd/C-190 catalyst had a high actual load ratio of approximately 87% (17.4%/20%) and the tiny Pd nanoparticles had an average particle size of approximately 3.5 nm. This was because a large number of intermediate-reducing substances produced by ethylene glycol and tert-butyl alcohol increased the nucleation rate of Pd nanoparticles at 190°C . Moreover, the electrochemical tests showed that the Pd/C-190 catalyst had a reliable activity and stability. The anode mass specific peak current density for the electro-oxidation of methanol and ethanol reached 687.4 and 1177.6 mA mg⁻¹ Pd, respectively. The reason that the Pd/C-190 catalyst had a good activity, and a high tolerance was related to its small Pd nanoparticles with good dispersion. Furthermore, its activity was greatly improved by the

small amount of Pd_xH_y components and abundant Pd (200) crystal faces of the Pd nanoparticles. Overall, the experimental scheme was efficient and convenient and was an ideal industrial method for the large-scale preparation of Pd/C catalysts with a high activity. The preparation of highly active Pd-based catalysts with this mixed solvent has a wide applicability and broad application prospects.

ACKNOWLEDGEMENT

We greatly appreciate the National Natural Science Foundation of China (51774017) and Major Science and Technology project of Shanxi (20181102019) to fund this work.

References

1. H. S. Liu, C. J. Song, L. Zhang, J. J. Zhang, H. J. Wang and D. P. Wilkinson, *J. Power Sources*, 155 (2006) 95.
2. Z. Dasdelen, Y. Yildiz, S. Eris and F. Sen, *Appl. Catal, B*, 219 (2017) 511.
3. O. Karatepe, Y. Yildiz, H. Pamuk, S. Eris, Z. Dasdelen and F. Sen, *RSC Adv*, 6 (2016) 50851.
4. A. Hamnett, *Catal. Today*, 38 (1997) 445.
5. Y. Li, W. Gao, L. Ci, C. Wang and P. M. Ajayan, *Carbon*, 48 (2010) 1124.
6. M.-k. Min, J. Cho, K. Cho and H. Kim, *Electrochim. Acta*, 45 (2000) 4211.
7. S. M. Choi, M. H. Seo, H. J. Kim and W. B. Kim, *Carbon*, 49 (2011) 904.
8. V. M. Chernyshev, A. V. Astakhov, I. E. Chikunov, R. V. Tyurin, D. B. Eremin, G. S. Ranny, V. N. Khrustalev and V. P. Ananikov, *ACS Catal*, 9 (2019) 2984.
9. E. Herrero, A. Fernández-Vega, J. M. Feliu and A. Aldaz, *J. Electroanal. Chem*, 350 (1993) 73.
10. K. Bergamaski, E. R. Gonzalez and F. C. Nart, *Electrochim. Acta*, 53 (2008) 4396.
11. J.-N. Zheng, M. Zhang, F.-F. Li, S.-S. Li, A.-J. Wang and J.-J. Feng, *Electrochim. Acta*, 130 (2014) 446.
12. D. Chen, P. Cui, H. He, H. Liu and J. Yang, *J. Power Sources*, 272 (2014) 152.
13. F. Bensebaa, A. A. Farah, D. Wang, C. Bock, X. Du, J. Kung and Y. Le Page, *J. Phys. Chem. B*, 109 (2005) 15339.
14. J. Fan, H. Du, Y. Zhao, Q. Wang, Y. Liu, D. Li and J. Feng, *ACS Catal.*, 10 (2020) 13560.
15. Y. Zhou, Z. Y. Wang and C. J. Liu, *Catal. Sci. Technol.*, 5 (2015) 69.
16. Y. Wang, S. Zou and W.-B. Cai, *Catal.*, 5 (2015) 1507.
17. R. Wang, S. Liao and S. Ji, *J. Power Sources*, 180 (2008) 205.
18. H. Erikson, A. Sarapuu, J. Solla-Gullón and K. Tammeveski, *J. Electroanal. Chem.*, 780 (2016) 327.
19. A. Lazzarini, A. Piovano, R. Pellegrini, G. Leofanti, G. Agostini, S. Rudic, M. R. Chierotti, R. Gobetto, A. Battiato, G. Spoto, A. Zecchina, C. Lamberti and E. Groppo, *Catal. Sci. Technol.*, 6 (2016) 4910.
20. R. M. Abdel Hameed, *Appl. Surf. Sci.*, 411 (2017) 91.
21. X.-m. Chen, Z.-j. Lin, D.-J. Chen, T.-t. Jia, Z.-m. Cai, X.-r. Wang, X. Chen, G.-n. Chen and M. Oyama, *Biosens. Bioelectron.*, 25 (2010) 1803.
22. X.-m. Chen, Z.-j. Lin, T.-t. Jia, Z.-m. Cai, X.-l. Huang, Y.-q. Jiang, X. Chen and G.-n. Chen, *Anal. Chim. Acta*, 650 (2009) 54.
23. H. Li, S. C. Zhang, S. H. Yan, Y. Lin and Y. B. Ren, *Int. J. Electrochem. Sci.*, 8 (2013) 2996.
24. L. Q. Lu, S. F. Yu, X. P. Yue, J. Wang, M. S. Liang, L. Z. Gao and S. H. Yan, *Int. J. Electrochem. Sci.*, 15 (2020) 7896.
25. Y. Zhao, X. Yang, J. Tian, F. Wang and L. Zhan, *Int. J. Hydrogen Energy*, 35 (2010) 3249.
26. M. Mougnot, A. Caillard, M. Simoes, S. Baranton, C. Coutanceau and P. Brault, *Appl. Catal., B*, 107 (2011) 372.

27. A. L. Thomann, J. P. Rozenbaum, P. Brault, C. Andreazza-Vignolle and P. Andreazza, *Appl. Surf. Sci.*, 158 (2000) 172.
28. S. Guo, S. Li, T. Hu, G. Gou, R. Ren, J. Huang, M. Xie, J. Jin and J. Ma, *Electrochim. Acta*, 109 (2013) 276.
29. S. Baek, K. H. Kim, M. J. Kim and J. J. Kim, *Appl. Catal., B*, 217 (2017) 313.
30. N. Tian, Z.-Y. Zhou, N.-F. Yu, L.-Y. Wang and S.-G. Sun, *J. Am. Chem. Soc.*, 132 (2010) 7580.
31. G. T. Fu, Z. Y. Liu, Y. Chen, J. Lin, Y. W. Tang and T. H. Lu, *Nano Res.*, 7 (2014) 1205.
32. Y. Xiong, J. Chen, B. Wiley, Y. Xia, S. Aloni and Y. Yin, *J. Am. Chem. Soc.*, 127 (2005) 7332.
33. Y. Zhao, L. Jia, J. A. Medrano, J. R. H. Ross and L. Lefferts, *ACS Catal.*, 3 (2013) 2341.
34. S. Yan and S. Zhang, *Int. J. Hydrogen Energy*, 36 (2011) 13392.
35. S. Y. Wang, N. Kristian, S. P. Jiang and X. Wang, *Nanotechnology*, 20 (2009) 2.
36. J. Panpranot, K. Kontapakdee and P. Praserttham, *Appl. Catal., A*, 314 (2006) 128.
37. D. Yuan, C. Xu, Y. Liu, S. Tan, X. Wang, Z. Wei and P. K. Shen, *Electrochem. Commun.*, 9 (2007) 2473.
38. J. Tang, J. Shen, N. Li and M. Ye, *Ceram. Int.*, 41 (2015) 6203.
39. D. K. Wen, Y. M. Wu, X. L. Ma, X. P. Yue, M. S. Liang, L. Z. Gao and S. H. Yan, *Int. J. Electrochem. Sci.*, 15 (2020) 4798.
40. Y. J. Yang, S. F. Yu, L. Z. Gao, X. M. Wang and S. H. Yan, *Int. J. Electrochem. Sci.*, 14 (2019) 1270.
41. B. Lin, X. Wu, L. Xie, Y. Kang, H. Du, F. Kang, J. Li and L. Gan, *Angew. Chem. Int. Ed.*, 59 (2020) 20348.
42. R. Bardhan, L. O. Hedges, C. L. Pint, A. Javey, S. Whitelam and J. J. Urban, *Nat. Mater.*, 12 (2013) 905.
43. A. L. Bugaev, A. A. Guda, K. A. Lomachenko, A. Lazzarini, V. V. Srabionyan, J. G. Vitillo, A. Piovano, E. Groppo, L. A. Bugaev, A. V. Soldatov, V. P. Dmitriev, R. Pellegrini, J. A. van Bokhoven and C. Lamberti, *J. Phys.: Conf. Ser.*, 712 (2016) 1.
44. Z. Zhao, X. Huang, M. Li, G. Wang, C. Lee, E. Zhu, X. Duan and Y. Huang, *J. Am. Chem. Soc.*, 137 (2015) 15672.
45. Y. Lu, J. Wang, Y. Peng, A. Fisher and X. Wang, *Adv. Energy Mater.*, 7 (2017) 21.
46. B. Lin, X. Wu, L. Xie, Y. Kang, H. Du, F. Kang, J. Li and L. Gan, *Angew. Chem., Int. Ed.*, 59 (2020) 20348.
47. D. Wen, Y. Wu, X. Ma, X. Yue, M. Liang, L. Gao and S. Yan, *Int. J. Electrochem. Sci.*, 15 (2020) 4798.
48. H. Li, S. Zhang, S. Yan, Y. Lin and Y. J. I. J. o. E. S. Ren, *Int. J. Electrochem. Sci.*, 8 (2013) 2996.
49. Q. Dong, Y. Zhao, X. Han, Y. Wang, M. C. Liu and Y. Li, *Int. J. Hydrogen Energy*, 39 (2014) 14669.
50. S. F. Yu, Q. Han, Y. J. Yang, X. L. Ma, L. Z. Gao, S. H. Yan, Y. C. Wu and L. Q. Lu, *Int. J. Electrochem. Sci.*, 14 (2019) 7871.
51. Z. Liu, J. Y. Lee, W. Chen, M. Han and L. M. Gan, *Liu, Z., Lee, J. Y., Chen, W., Han, M., & Gan, L. M., Langmuir*, 20 (2004) 181.
52. S. Yan, S. Zhang, W. Zhang, J. Li, L. Gao, Y. Yang and Y. Gao, *J. Phys. Chem. C.*, 118 (2014) 29845.
53. J. A. Barnard, *Trans. Faraday Soc.*, 55 (1959) 947.
54. X. Li, W. X. Chen, J. Zhao, W. Xing and Z. D. Xu, *Carbon*, 43 (2005) 2168.
55. X. J. Zhu, H. L. Dai, J. Hu, L. Ding and L. Jiang, *J. Power Sources*, 203 (2012) 243.
56. Jianxin, Wu, Jiang Bohong, and T. Y. Hsu, *Acta Metall.*, 36.6 (1988)1521.
57. G. H. Liu, L. X. Wang, Y. W. T. Hu, C. H. Sun, H. Y. Leng, Q. Li and C. Z. Wu, *J. Alloys Compd.*, 881 (2021) 1.
58. F.P. Hu and P.K. Shen, *J. Power Sources*, 173 (2007) 877.

59. C. Li, S. H. Yan and J. Y. Fang, *Small*, 17 (2021) 46 .
60. Z. Xia and S. Guo, *Chem. Soc. Rev.*, 48 (2019) 3265.
61. R. Chattot, T. Asset, P. Bordet, J. Drnec, L. Dubau and F. Maillard, *ACS Catal.*, 7(2017) 398.
62. H. J. Huang and X. Wang, *J. Mater. Chem.*, 22 (2012) 22533.
63. S. H. Yan, S. C. Zhang, Y. Lin and G. R. Liu, *J. Phys. Chem. C.*, 115 (2011) 6986.
64. C. S. Shang, W. Hong, Y. X. Guo, J. Wang and E. K. Wang, *Chem. Eur. J.*, 23 (2017) 5799.
65. W. Hong, P. Y. Bi, C. S. Shang, J. Wang and E. K. Wang, *J. Mater. Chem. A*, 4 (2016) 4485.
66. Y. Xia, Y. Xiong, B. Lim and S. E. Skrabalak, *Angew. Chem. Int. Ed.*, 48 (2009) 60.
67. S. Fonseca, G. Maia and L. M. C. Pinto, *Electrochem. Commun.*, 93 (2018) 100.
68. Y. Wang, Y. Zhao, J. Yin, M. C. Liu, Q. Dong and Y. Q. Su, *Int. J. Hydrog. Energy*, 39 (2014) 1325.
69. J. Fan, X. Cui, S. Yu, L. Gu, Q. Zhang, F. Meng, Z. Peng, L. Ma, J.-Y. Ma, K. Qi, Q. Bao and W. Zheng, *ACS nano*, 13 (2019) 12987.
70. P. S. Bagus and C. Björkman, *Phys. Rev. A*, 23 (1981) 461.
71. S. Dutta, C. Ray, A. Roy, R. Sahoo and T. Pal, *Chem. Eur. J.*, 22 (2016) 10017.
72. L. Jiang, A. Hsu, D. Chu and R. Chen, *Int. J. Hydrog. Energy*, 35 (2010) 365.
73. Y. N. Xia, Y. J. Xiong, B. Lim and S. E. Skrabalak, *Angew. Chem. Int. Ed.*, 48 (2009) 60.
74. C. Li, X. Chen, L. Zhang, S. Yan, A. Sharma, B. Zhao, A. Kumbhar, G. Zhou and J. Fang, *Angew. Chem., Int. Ed. Engl.*, 60 (2021) 7675.
75. W. Ye, Y. Chen, Y. Zhou, J. Fu, W. Wu, D. Gao, F. Zhou, C. Wang and D. Xue, *Electrochim. Acta*, 142 (2014) 18.
76. A. N. Simonov, P. A. Pyrjaev, P. A. Simonov, B. L. Moroz, S. V. Cherepanova, D. A. Zyuzin, V. I. Bukhtiyarov and V. N. Parmon, *J. Mol. Catal. A: Chem.*, 353-354 (2012) 204.
77. S. Yan, S. Zhang, Y. Lin and G. Liu, *J. Phys. Chem. Lett.*, 115 (2011) 6986.
78. S. Zhang, Y. Y. Shao, G. P. Yin and Y. H. Lin, *J. Power Sources*, 195 (2010) 1103.
79. M. Kissia, M. Bouklah, B. Hammouti and M. Benkaddoura, *Appl. Surf. Sci.*, 252(2006), 4190.
80. D. A. Aikens, *J Chem Educ*, 60 (1983) A25.
81. A. Schwake, H. Geuking and K. Cammann, *Electroanalysis*, 10 (1998) 1026.